



## Tumor-targeting hyaluronic acid nanoparticles for photodynamic imaging and therapy

Hong Yeol Yoon<sup>a,1</sup>, Heebeom Koo<sup>b,1</sup>, Ki Young Choi<sup>b</sup>, So Jin Lee<sup>b</sup>, Kwangmeyung Kim<sup>b</sup>, Ick Chan Kwon<sup>b</sup>, James F. Leary<sup>c</sup>, Kinam Park<sup>c</sup>, Soon Hong Yuk<sup>d</sup>, Jae Hyung Park<sup>a,\*</sup>, Kuiwon Choi<sup>b,\*\*</sup>

<sup>a</sup> Department of Polymer Science and Engineering, Sungkyunkwan University, Suwon 440-746, Republic of Korea

<sup>b</sup> Center for Theragnosis, Biomedical Research Institute, Korea Institute of Science and Technology (KIST), Hwarangno 14-gil 6, Seongbuk-gu, Seoul 136-791, Republic of Korea

<sup>c</sup> Departments of Biomedical Engineering, Purdue University, West Lafayette, IN 47907, USA

<sup>d</sup> College of Pharmacy, Korea University, Jochiwon, Yeongi, Chungnam 339-700, Republic of Korea

### ARTICLE INFO

#### Article history:

Received 14 December 2011

Accepted 6 February 2012

Available online 24 February 2012

#### Keywords:

Photodynamic therapy

Imaging

Tumor-targeting

Nanoparticle

Hyaluronic acid

Chlorin e6

### ABSTRACT

Tumor-targeted imaging and therapy have been the challenging issue in the clinical field. Herein, we report tumor-targeting hyaluronic acid nanoparticles (HANPs) as the carrier of the hydrophobic photosensitizer, chlorin e6 (Ce6) for simultaneous photodynamic imaging and therapy. First, self-assembled HANPs were synthesized by chemical conjugation of aminated 5 $\beta$ -cholanolic acid, polyethylene glycol (PEG), and black hole quencher3 (BHQ3) to the HA polymers. Second, Ce6 was readily loaded into the HANPs by a simple dialysis method resulting in Ce6-loaded hyaluronic acid nanoparticles (Ce6-HANPs), wherein the loading efficiency of Ce6 was higher than 80%. The resulting Ce6-HANPs showed stable nano-structure in aqueous condition and rapid uptake into tumor cells. In particular Ce6-HANPs were rapidly degraded by hyaluronidases abundant in cytosol of tumor cells, which may enable intracellular release of Ce6 at the tumor tissue. After an intravenous injection into the tumor-bearing mice, Ce6-HANPs could efficiently reach the tumor tissue via the passive targeting mechanism and specifically enter tumor cells through the receptor-mediated endocytosis based on the interactions between HA of nanoparticles and CD44, the HA receptor on the surface of tumor cells. Upon laser irradiation, Ce6 which was released from the nanoparticles could generate fluorescence and singlet oxygen inside tumor cells, resulting in effective suppression of tumor growth. Overall, it was demonstrated that Ce6-HANPs could be successfully applied to *in vivo* photodynamic tumor imaging and therapy simultaneously.

© 2012 Elsevier Ltd. All rights reserved.

### 1. Introduction

In tumor diagnosis and therapy, one of the most essential challenges is enhancing the target-specificity of imaging and therapeutic agents [1,2]. To accomplish this purpose, tumor-targeted delivery systems for them have been received much attention by biomedical researchers [3]. Tumor-targeted imaging systems are expected to provide the enhanced signal at the tumor tissue with the minimal background noise [4]. Also, tumor-targeted drug delivery systems may lead to an efficient suppression of tumor growth and minimize the side effects in other organs [5]. However, it is difficult to develop such ideal systems because there are many

obstacles for tumor-targeting in the body such as the reticuloendothelial system of liver and spleen [6].

Over the last decade, numerous nanoparticles have been developed for *in vivo* tumor-targeted delivery of imaging agents or drugs [7,8]. In our research group, hyaluronic acid nanoparticles (HANPs) have been investigated for tumor therapy and imaging because of their tumor-targeting ability *in vivo* [9,10]. It has been demonstrated that, after systemic administration, they can effectively reach the tumor site based on the enhanced permeability and retention (EPR) effect as well as active targeting mechanism via binding of HA to CD44, the HA receptor over-expressed on tumor cells [11,12]. Furthermore, CD44 has received attention as the target receptor for cancer therapy since it plays pivotal roles in cancer stem-like cells and resistance to chemotherapy or radiotherapy [13,14]. Another unique feature of HANPs is that they can be rapidly degraded by hyaluronidases abundant in cytosol of tumor cells, which may enable fast release of inner cargos [15,16]. We also demonstrated that tumor-targeting ability of HANPs could be

\* Corresponding author. Tel.: +82 31 299 6859; fax: +82 31 292 8790.

\*\* Corresponding author. Tel.: +82 2 958 5921; fax: +82 2 958 5909.

E-mail addresses: [jhpark1@skku.edu](mailto:jhpark1@skku.edu) (J.H. Park), [choi@kist.re.kr](mailto:choi@kist.re.kr) (K. Choi).

<sup>1</sup> These authors contributed equally to this paper.

optimized by chemical conjugation of polyethylene glycol (PEG), which might help escaping the unintended accumulation in liver [17]. These characteristics of HANPs make them attractable for *in vivo* tumor-targeted delivery of imaging agents or drugs.

Herein, we hypothesized that HANPs could be used as the tumor-targeted delivery system of photosensitizers for both photodynamic imaging (PDI) and photodynamic therapy (PDT). Because photosensitizers can generate fluorescence for imaging and singlet oxygen for therapy simultaneously upon irradiation, it may be useful as theragnostic system for combined diagnosis and therapy [18,19]. For this purpose, HANPs were further modified by polyethylene glycol (PEG) and black hole quencher3 (BHQ3), and the hydrophobic photosensitizer, chlorin e6 (Ce6) was loaded into these nanoparticle resulting in Ce6-loaded hyaluronic acid nanoparticles (Ce6-HANPs). Thereafter, we evaluated the release of Ce6, its dequenching behavior, and singlet oxygen generation from Ce6-HANPs in presence of hyaluronidase which is abundant in cytosol of tumor cells. The tumor cell-specific fluorescence and singlet oxygen generation from Ce6-HANPs was also proved in cellular imaging and cell viability test. In addition, the *in vivo* tumor-targeted imaging and therapeutic efficacy of Ce6-HANPs were evaluated using the tumor-bearing mice models.

## 2. Materials and methods

### 2.1. Materials

Sodium hyaluronate (MW =  $2.34 \times 10^5$  Da) was purchased from Lifecore Biomedical LLC (Chaska, USA). 5 $\beta$ -cholic acid, 1-ethyl-3(3-dimethylaminopropyl) carbodiimide (EDC), N-hydroxysuccinimide (NHS), N,N-dimethyl-4-nitrosoaniline (RNO), L-histidine, dimethylsulfoxide (DMSO), tetrahydrofuran (THF), and thiazolyl blue tetrazolium bromide (MTT) were purchased from Sigma-Aldrich Co (St. Louis, MO, USA). Monomethoxy PEG amine (MW =  $5 \times 10^3$  Da) was obtained from Lysan Bio Inc (Alabama, USA). Black hole quencher3 amine (BHQ3) was purchased from Biosearch Technologies Inc (Novato, USA), and chlorin e6 (Ce6) was obtained from Frontier Scientific Inc (Logan, USA). Hyaluronidase (Hyal-1, 240 N.F.U/mg) was purchased from TCI (Tokyo, Japan). Trypan blue solution was purchased from Gibco (Grand Island, NY, USA). All other chemicals were analytical grade and used without further purification. HT29 human colon cancer cell and NIH3T3 mouse embryo fibroblast cells were purchased from the American Type Culture Collection (Rockville, MD, USA).

### 2.2. Preparation of Ce6-loaded hyaluronic acid nanoparticles (Ce6-HANPs)

Amphiphilic PEGylated HA conjugates were synthesized using HA, aminated 5 $\beta$ -cholic acid, and amine-functionalized PEG as described previously [17]. All products were purified by dialysis after each synthetic step, which was confirmed using  $^1\text{H}$  NMR (UnityPlus300, Varian, CA, USA). Aminated BHQ3 was also conjugated to these conjugates as follows. PEGylated HA conjugates (20 mg) were dissolved in 5 ml of 1:1 (v/v) DMSO/distilled water solution, followed by mixing with NHS (1.3 mg) and EDC (0.8 mg). Aminated BHQ3 (2.4 mg) in 1.0 ml of DMSO was slowly added to the solution. After vigorous stirring for 24 h at room temperature, the solution was purified by dialysis against methanol and distilled water for three days using the dialysis tube (MW cutoff = 12 kDa–14 kDa, Spectrum®, Rancho Dominguez, CA) and was lyophilized to obtain the violet powder. The chemical structure of final product, HANP was also analyzed using  $^1\text{H}$  NMR. The characteristic peaks of 5 $\beta$ -cholic acid, PEG, and HA were at 0.6–1.8 ppm, 3.6 ppm, and 2.0 ppm, respectively, and their integration peak ratios were calculated as described previously [17].

Ce6 was loaded into HANP using a simple dialysis method. In brief, pre-determined amount of Ce6 (2.0–8.0 mg) in 1 ml of 1:1 (v/v) THF/distilled water was slowly added to HANP (20 mg) dissolved in 4 ml of the same co-solvent. Thereafter, the solution was sonicated three times for 1 min each using a probe type sonicator (VCX-750, Sonics & Materials, CT, USA) and was dialyzed for 6 h against water using dialysis membrane (MW cutoff = 12 kDa–14 kDa). After filtering with 0.8  $\mu\text{m}$  syringe filter to remove unloaded Ce6, the solution was lyophilized to obtain the green powder, Ce6-HANP.

### 2.3. Characterization of Ce6-HANPs

The amount of conjugated BHQ3 and loaded Ce6 in Ce6-HANPs were determined using the UV–VIS spectrometer (G1103A, Agilent, USA) by measuring absorbance at 405 nm ( $\lambda_{\text{max}}$  of Ce6) and 630 nm ( $\lambda_{\text{max}}$  of BHQ3), respectively. All samples were prepared by dissolving in 1:1 (v/v) DMSO/distilled water and were

analyzed based on a standard curve of free BHQ3 and Ce6. To measure the size distribution of Ce6-HANPs by dynamic light scattering (DLS, 90 Plus, Brookhaven Instruments Corporation, USA), the samples were dissolved in PBS (pH 7.4, 1.0 mg/ml) and sonicated for 5.0 min using the probe-type sonicator (VCX-750, Sonics & Materials) at 180 W. The morphology of Ce6-HANPs was observed using the transmission electron microscopy (TEM, Philips CM30) at an accelerating voltage of 200 kV. For TEM images, samples were dispersed in distilled water and dropped on the 200 mesh copper grid. All samples were stained by 1% uranyl acetate for negative staining.

### 2.4. *In vitro* Ce6 release test

To determine the release behavior of Ce6 from nanoparticles, Ce6-HANPs were dispersed in PBS (pH 7.4, 1.0 mg/ml) with and without 120 unit/ml of Hyal-1. The dispersed Ce6-HANPs solutions were transferred to the dialysis membrane tube (MW cutoff = 100 kDa). The resulting tube was placed in 20 ml of PBS with 0.1% (w/v) tween80 to set the sink condition of Ce6 and was gently shaken at 150 rpm in water bath at 37 °C. The medium was changed with fresh medium at pre-determined time points. To measure the released amount of Ce6 from nanoparticles, 1.0 ml of the release medium was taken at pre-determined time points and DMSO (1 w/v % based on the medium) was added. The concentration of Ce6 was analyzed using UV–Vis spectrometer by measuring the absorbance at 405 nm, based on a standard curve of free Ce6.

### 2.5. *In vitro* measurement of fluorescence quenching and dequenching

To evaluate the fluorescence quenching and dequenching of Ce6-Q-P-HANPs, they were dispersed in PBS (pH 7.4, 37 °C) with and without 120 unit/ml of Hyal-1, and each sample was loaded onto 4-face transparent quartz cuvette. The fluorescence intensity of Ce6 was obtained using fluorescence spectrophotometer (F-7000, Hitachi, Tokyo, Japan). The fluorescence images of Ce6 at various concentrations of Hyal-1 were observed using 12-bit CCD camera (Kodak Image Station 4000MM, New Haven, CT, USA). Total fluorescence intensity in a region of interests (1450 pixel per ROI) was calculated with Kodak MI software (New Haven, CT, USA).

### 2.6. *In vitro* measurement of singlet oxygen generation

The generation of singlet oxygen from Ce6 was quantitatively evaluated using RNO as a singlet oxygen sensor [20]. Free Ce6 (100  $\mu\text{g}/\text{ml}$ ) and Ce6-HANPs (100  $\mu\text{g}/\text{ml}$  of Ce6) in 200  $\mu\text{l}$  of 1% DMSO solution in distilled water were added to 3.8 ml of distilled water containing 5.58 mg of L-histidine and 0.377  $\mu\text{g}$  of RNO with and without 120 unit/ml of Hyal-1. Then, each solution was located in 1 ml quartz cuvette and irradiated using 671 nm He-Ne laser (DPSS 671 nm Red Laser, i-Nexus, Inc.). The absorbance of RNO was measured at 405 nm using UV–Vis spectrometer as a function of time.

### 2.7. Cellular imaging

HT29 and NIH3T3 cells were cultured in RPMI1640 and DMEM medium (Gibco, Grand Island, NY, USA) containing 10% fetal bovine serum and 1% penicillin-streptomycin at 37 °C in a CO<sub>2</sub> incubator. To determine cellular uptake of Ce6s, HT29 cells and NIH3T3 cells ( $1 \times 10^5$  cells/well) were seeded onto 6-well plates and stabilized for 24 h. For competitive inhibition study, 8 mg/ml of HA polymer was co-treated with Ce6-HANPs on HT29 cells. The fluorescence images were observed using 12-bit CCD camera, and total fluorescence intensity was calculated as described above.

To obtain high-resolution intracellular images, HT29 cells and NIH3T3 cells ( $1 \times 10^5$  cells/well) were seeded onto gelatin coated cover slip in 6-well plates, and they were treated with serum-free medium containing free Ce6 or Ce6-HANP (20  $\mu\text{g}/\text{ml}$  of free Ce6) for 5–30 min at 37 °C in a CO<sub>2</sub> incubator. The cells were then washed twice with Dulbecco's PBS (DPBS) and fixed with a 4% paraformaldehyde solution. After 4,6-diamidino-2-phenylindole (DAPI) mounting, HT29 and NIH3T3 cells were observed using a confocal laser microscope (FV10i, Olympus, USA).

### 2.8. Cell viability assays

To determine cell viability under dark condition, HT29 and NIH3T3 cells ( $1 \times 10^4$  cells/well) were seeded onto 96-well plates and incubated for 24 h. After cell stabilization, the culture medium was replaced with 200  $\mu\text{l}$  of serum-free medium containing free Ce6 or Ce6-HANPs (0–20  $\mu\text{g}/\text{ml}$  of Ce6), followed by incubation for 30 min at 37 °C. The cells were then washed twice with serum-free culture medium and cell viability was evaluated by the MTT assay.

To determine cell viability after laser irradiation, HT29 cells and NIH3T3 cells were seeded on 96-well plates ( $1 \times 10^4$  cells/well), and treated with serum-free culture medium free Ce6 or Ce6-HANPs (0–20  $\mu\text{g}/\text{ml}$  of Ce6). After 30 min incubation, the cells were washed twice with serum-free medium and irradiated with a 671 nm He-Ne laser (100 mW/cm<sup>2</sup>) for 0–4 min onto the 96-well plates. After 6 h incubation, cell viability of irradiated cells was evaluated by the MTT assay.

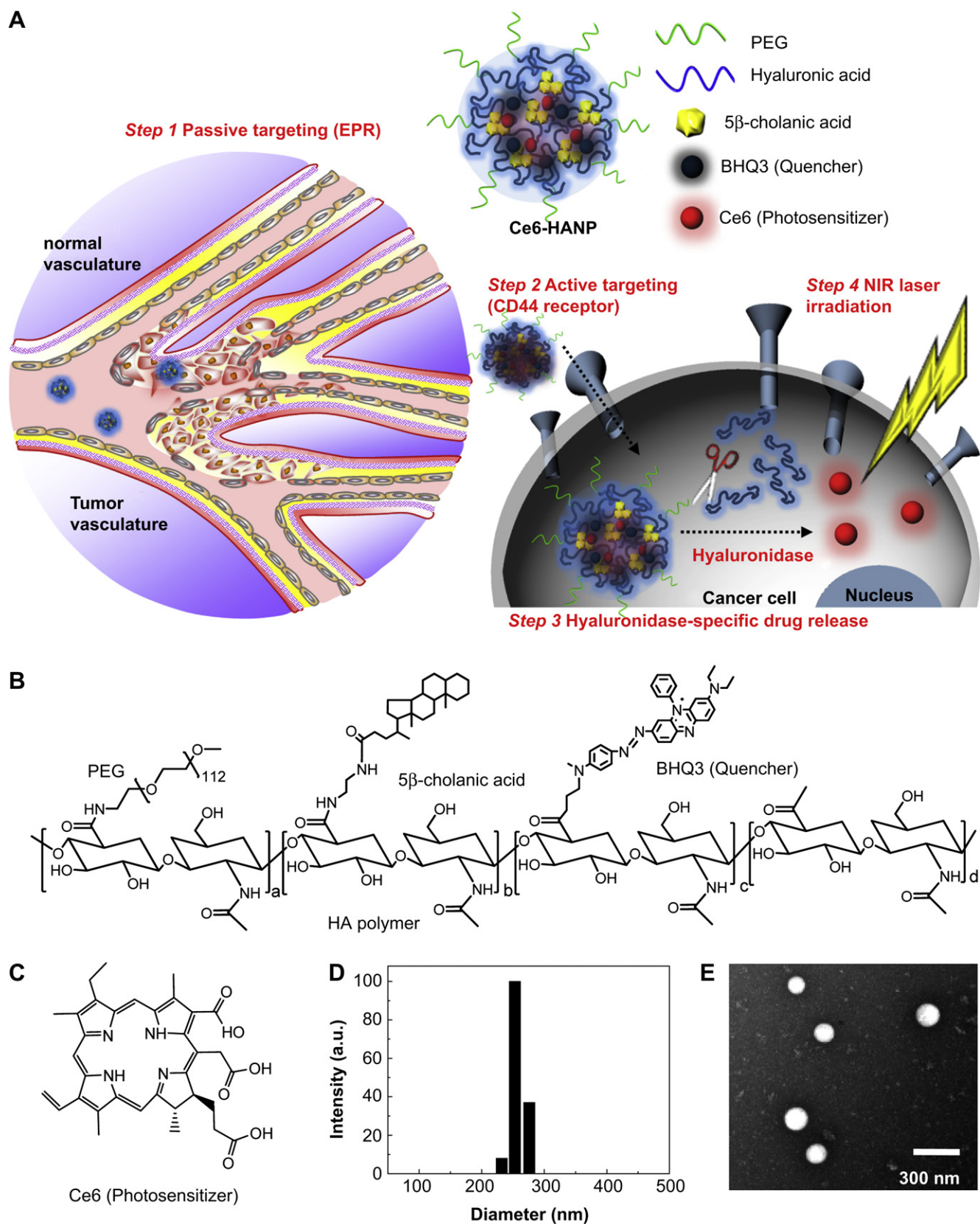


**Fig. 1.** Development and characterization of tumor-targeting hyaluronic acid nanoparticle containing Ce6 (Ce6-HANP) for photodynamic imaging and therapy. (A) Schematic illustration of Ce6-HANP as tumor-targeted delivery system for simultaneous photodynamic imaging and therapy. (B) Chemical structure of HANP. (C) Chemical structure of chlorin e6 (Ce6) as photosensitizer. (D) Size distribution of Ce6-HANP by dynamic light scattering (DLS). (E) Transmission electron microscopy (TEM) images of Ce6-HANP.

To observe dead cells, trypan blue staining was performed for the cells on the 6-well plates ( $1 \times 10^5$  cells/well). After laser irradiation for 2 min, both cells were washed twice with DPBS and treated with 0.5 ml of the trypan blue solution (0.4% in PBS, pH 7.4) for 5 min. The solution was then washed using DPBS for three times, and cells were fixed with 4% paraformaldehyde solution. Dead cells were observed using an optical microscope (BX51, Olympus, USA).

### 2.9. *In vivo* and *ex vivo* fluorescence imaging

All experiments with live animals were performed in compliance with the relevant laws and institutional guidelines of Korea Institute of Science and Technology (KIST), and institutional committees have approved the experiments. To observe biodistribution of Ce6 in an animal model, tumor-bearing athymic nude mice (4.5-weeks old, 20–25 g, male) were prepared by inoculating a suspension of  $1 \times 10^7$  HT29 cells in saline (60  $\mu$ l) into left flanks of mice. When tumors grew to approximately 250–500 mm<sup>3</sup> in volume, 200  $\mu$ l of PBS containing free Ce6 or Ce6-HANPs (5 mg/kg of Ce6) were injected into the mice via tail vein ( $n = 3$  per each group). The *in vivo* biodistribution of Ce6 were imaged using the eXplore Optix system with 670 nm-pulsed laser diode (ART Advanced Research Technologies Inc., Montreal, Canada) [21]. To observe the organ distribution of Ce6, another groups of mice were prepared and treated by same procedures ( $n = 3$  per each groups). They were then sacrificed at 24 h post-injection, and major organs and tumors were excised and observed by the Kodak image station (Kodak Image Station 4000MM, New Haven, CT, USA) [22]. All the near infrared fluorescence (NIRF) intensities were calculated using the Analysis Workstation software (ART Advanced Research Technologies Inc., Montreal, Canada).

### 2.10. *In vivo* photodynamic therapy and histology

Tumor-bearing mice models were prepared in an identical manner as described above. When tumors grew up to  $55 \pm 10$  mm<sup>3</sup> in volume, 200  $\mu$ l of saline, PBS containing free Ce6 or Ce6-HANPs were injected into the mice via tail vein ( $n = 4$  per each group). At 4 h and 24 h post-injections, tumor tissues were irradiated by 671 nm He-Ne laser (100 mW/cm<sup>2</sup>) for 30 min. After irradiation, the therapeutic results of each group were evaluated by measuring the tumor volumes for 12 days. For histological analysis, tumor tissues were excised from the mice at 12 days post-injection, and they were fixed with 2% paraformaldehyde solution and embedded in paraffin. The sliced tumor tissues (6  $\mu$ m) were stained by Hematoxylin and Eosin (H&E) and observed by optical microscope.

### 2.11. Statistics

The differences between experimental and control groups were analyzed using one-way ANOVA and considered statistically significant (marked with an asterisk (\*) in figures) if  $p < 0.05$ .

## 3. Results and discussion

### 3.1. Preparation and characterization of Ce6-HANPs

Fig. 1A shows our four-step-strategy for *in vivo* photodynamic imaging and therapy using Ce6-HANPs as tumor-targeted delivery system. First, Ce6-HANPs may efficiently reach the target tumor tissue by the EPR effect for their stable nano-structure after systemic administration [11]. Second, they can be easily taken up by the tumor cells via CD44 receptor-mediated endocytosis. Third, loaded Ce6 can be released from nanoparticles through degradation of the HA backbone by hyaluronidase abundant in cytosol of tumor cells [23]. Finally, the released Ce6 can recover their fluorescence for tumor imaging and generate singlet oxygen for tumor therapy upon laser irradiation focused on tumor site. These steps were rationally designed to enhance the specificity of PDT.

HANPs were synthesized by the conjugation of hydrophobic 5 $\beta$ -cholic acid groups to hydrophilic HA backbone, and they were further modified with adequate amount of PEG as described previously [17]. In this study, BHQ3 was additionally conjugated to HANPs because it can effectively quench fluorescent molecules like Ce6 [24,25]. The resulting conjugate, shown in Fig. 1B, could be self-assembled into nanoparticles in the aqueous condition because of its amphiphilic property. Its average size was determined to  $227.1 \pm 12.5$  nm, as determined using DLS. The characteristics of HANPs are shown in Table 1.

**Table 1**  
Characteristics of HANP.

M <sub>w</sub> of HA <sup>a</sup>	D.S. of 5 $\beta$ -cholic acid (%) <sup>b</sup>	D.S. of mPEG <sub>5000</sub> (%) <sup>b</sup>	D.S. of BHQ3 (%) <sup>c</sup>	Mean Diameter (nm) <sup>d</sup>
234.4 kDa	7.85 $\pm$ 0.38	4.47 $\pm$ 0.89	2.9 $\pm$ 0.30	227.1 $\pm$ 12.5

<sup>a</sup> Weight average molecular weight, measured using gel permeation chromatography (GPC).

<sup>b</sup> Mole ratio to sugar residue of HA, estimated from <sup>1</sup>H NMR spectrum.

<sup>c</sup> Mole ratio to sugar residue of HA, estimated using the UV-VIS spectrometer.

<sup>d</sup> Measured using dynamic light scattering (DLS).

As photosensitizer, Ce6 was chosen in this study because of its high singlet oxygen quantum yield and absorption/emission wavelength in NIR region with relatively efficient tissue penetration (Fig. 1C) [26,27]. Ce6 was readily loaded by the simple dialysis method. At 10% feed ratio of Ce6, the loading efficacy was 84.1%, but it decreased to 61.9% at 20% feed ratio (Table 2). Furthermore, it was lower than 50% in case of over 30% feed ratio (data not shown). Consequently, we used Ce6-HANPs of 10% Ce6 feed ratio for further studies. The size of Ce6-HANPs was  $250.7 \pm 13.6$  nm, suggesting that the particle size of HANPs slightly increases by incorporation of Ce6 (Fig. 1D). Their sizes and spherical shapes were also confirmed by the TEM image (Fig. 1E). This particle size, smaller than 300 nm, was demonstrated to be advantageous for high accumulation in tumor tissue with fenestrate vascular structure by the EPR effect [28].

### 3.2. Release behavior and singlet oxygen generation of Ce6 from Ce6-HANPs

Release pattern of Ce6 from Ce6-HANPs was evaluated with or without Hyal-1 which is the representative hyaluronidase in cytosol of tumor cells and plays pivotal role in HA turn over [29]. As shown in Fig. 2A, the release rate of Ce6 was much higher in the presence of Hyal-1, suggesting that Ce6-HANPs can rapidly release Ce6 in cytosol of tumor cells because the HA backbone of Ce6-HANPs is highly susceptible to Hyal-1 [30,31].

The fluorescence signals of free Ce6 and Ce6-HANPs at various concentrations of Hyal-1 were determined to observe the dequenching effect (Fig. 2B). As expected, free Ce6 exhibited strong fluorescence signals, whereas no significant changes in the intensity were found at different concentrations of Hyal-1. The fluorescence intensity of Ce6-HANPs was much lower in the absence of Hyal-1 than that of free Ce6, which is due to BHQ3 in Ce6-HANPs and self-quenching. It is of interest to note that the fluorescence intensity of Ce6-HANPs was highly enhanced as the concentration of Hyal-1 increased (Fig. 2C). At 120 unit/ml of Hyal-1, the fluorescence intensity of Ce6-HANPs was comparable to that of free Ce6. This is due to dequenching of Ce6 by its rapid release from nanoparticles.

Photosensitizers generate singlet oxygen for killing tumor cells upon laser irradiation, and the amount of singlet oxygen can be analyzed by measuring the decrease in absorbance of RNO (singlet oxygen sensor) [20]. Fig. 2D shows the RNO concentration as a function of time at various conditions. In the absence of Hyal-1,

**Table 2**  
Characteristics of Ce6-HANP after Ce6 loading.

Ce6 feed ratio (%) <sup>a</sup>	Loading contents (%) <sup>b</sup>	Loading efficiency (%)	Mean Diameter (nm) <sup>c</sup>
10	8.4 $\pm$ 0.29	84.1 $\pm$ 2.92	250.7 $\pm$ 13.6
20	12.4 $\pm$ 0.03	61.9 $\pm$ 0.15	245.5 $\pm$ 20.2

<sup>a</sup> Weight feed ratio to HANP.

<sup>b</sup> Weight contents of Ce6 in Ce6-HANP, estimated using the UV-VIS spectrometer.

<sup>c</sup> Measured using dynamic light scattering (DLS).

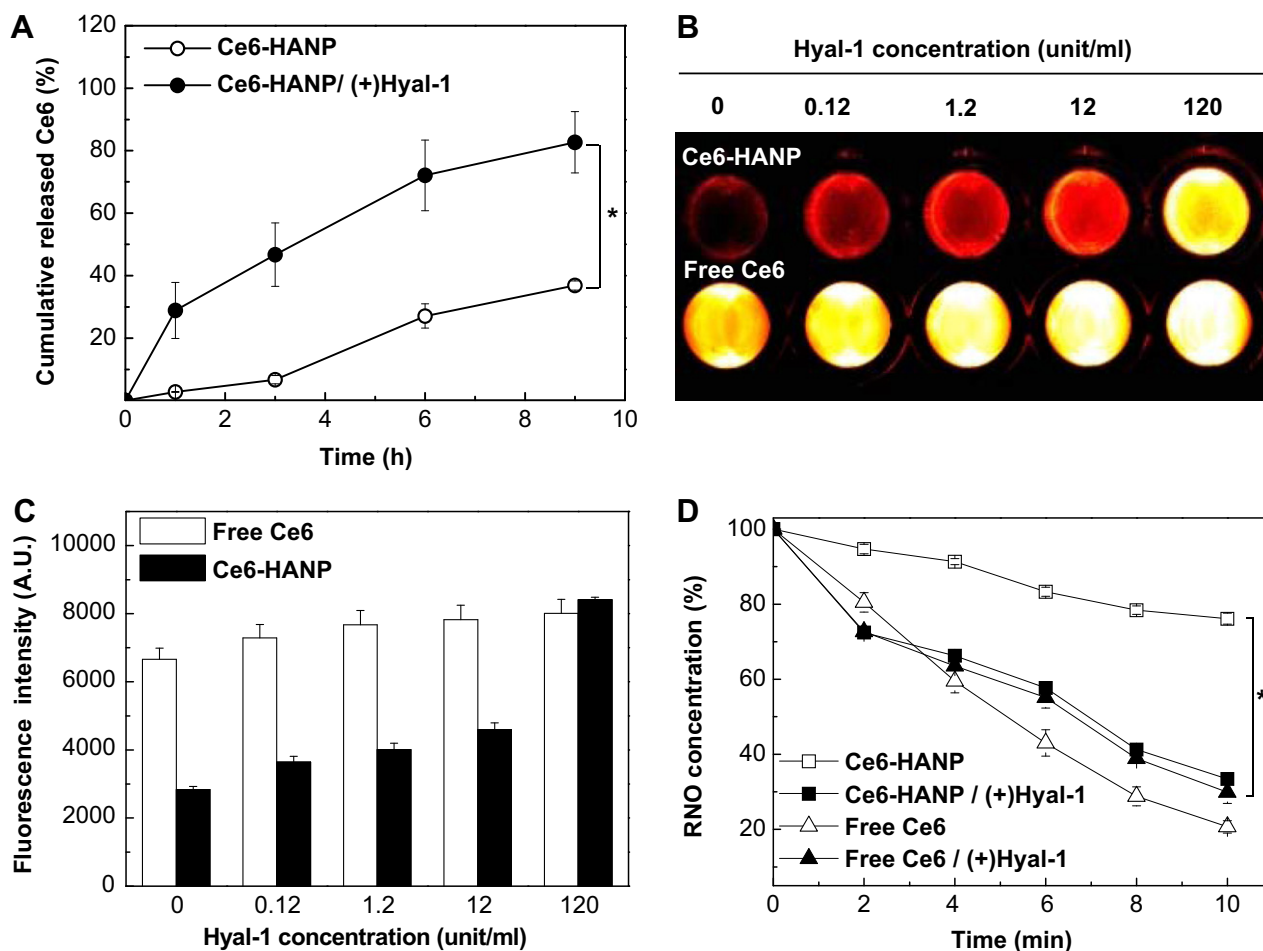


**Fig. 2.** *In vitro* hyaluronidase (Hyal-1) triggered Ce6 release and singlet oxygen generation of Ce6-HANP. (A) Release profile of Ce6-HANP with or without Hyal-1 (120 unit/ml). \*indicates difference at the  $p < 0.05$  significance level. (B) Fluorescence images of free Ce6 and Ce6-HANP after treatment of Hyal-1. (C) Fluorescence intensity of (B). (D) Singlet oxygen generation from free Ce6 and Ce6-HANP with or without Hyal-1 (120 unit/ml). \*indicates difference at the  $p < 0.05$  significance level.

the rate of singlet oxygen generation from Ce6-HANPs was significantly lower than that of free Ce6. This suggests that BHQ3 in nanoparticles could effectively suppress singlet oxygen generation by the photosensitizer. On the other hand, singlet oxygen generation from Ce6-HANPs was much faster in presence of Hyal-1, implying the fast recovery of therapeutic ability by enzymes abundant inside tumor cells.

### 3.3. Cellular uptake and intracellular fluorescence generation of Ce6-HANPs

Next, we observed the specific uptake and dequenching of Ce6-HANPs in tumor cells via fluorescence cellular imaging. NIH3T3 and HT29 were chosen as normal tissue cell line and tumor cell line, respectively. As shown in Fig. 3A, stronger fluorescence was observed in HT29 cells than in NIH3T3 cells after incubation with Ce6-HANPs. At 30 min incubation, the fluorescence intensity of Ce6 in HT29 cells was 4.1 fold higher than that in NIH3T3 cells (Fig. 3B). In case of free Ce6, the difference of fluorescence between two cell lines was negligible. It should be emphasized that the fluorescence intensity of Ce6 in HT29 cells remarkably decreased when Ce6-HANPs were incubated with excess amount of free HA, indicating that the specific uptake of Ce6-HANPs into tumor cells was based on binding of nanoparticles to CD44. With confocal microscopy and DAPI staining, intracellular distribution of Ce6 after cellular uptake was more precisely observed. In Fig. 3C, the fast uptake of Ce6-

HANPs was shown in HT29 tumor cells, in which loaded Ce6 was released and generated fluorescence. The red spots of Ce6 from Ce6-HANP were widely spread in cytoplasm. Because the main target of photodynamic therapy is major cellular organelles in cytoplasm, this result implies that the therapeutic efficacy of Ce6-HANPs may not be disturbed by unintended intracellular distribution [32].

### 3.4. NIR laser-triggered cellular phototoxicity

The photosensitizer does not exhibit cytotoxicity in the absence of light, whereas it generates singlet oxygen for therapy by the irradiation with an appropriate wavelength [18]. As expected, both free Ce6 and Ce6-HANPs showed negligible cytotoxicity on HT29 and NIH3T3 cells under dark condition, which was demonstrated by the MTT assay (Fig. 4A). Because HANPs were prepared using HA found in human body, they did not show negative effects on cell viability. However, the number of living cells remarkably decreased after irradiation with a 671 nm He-Ne laser (Fig. 4B). In case of free Ce6, the degree of phototoxicity was similar in both HT29 and NIH3T3 cells. On the contrary, Ce6-HANPs did specific damage to tumor cells. For HT29 cells treated with Ce6-HANPs, the viability was lower than 10% after a 2 min irradiation with NIR laser. However, more than 70% of NIH3T3 cells, treated with Ce6-HANPs, survived at the same condition. This result suggests the laser-induced phototoxicity of Ce6-HANPs is tumor cell-specific, which is consistent with the results in cellular imaging. Interestingly, the phototoxicity

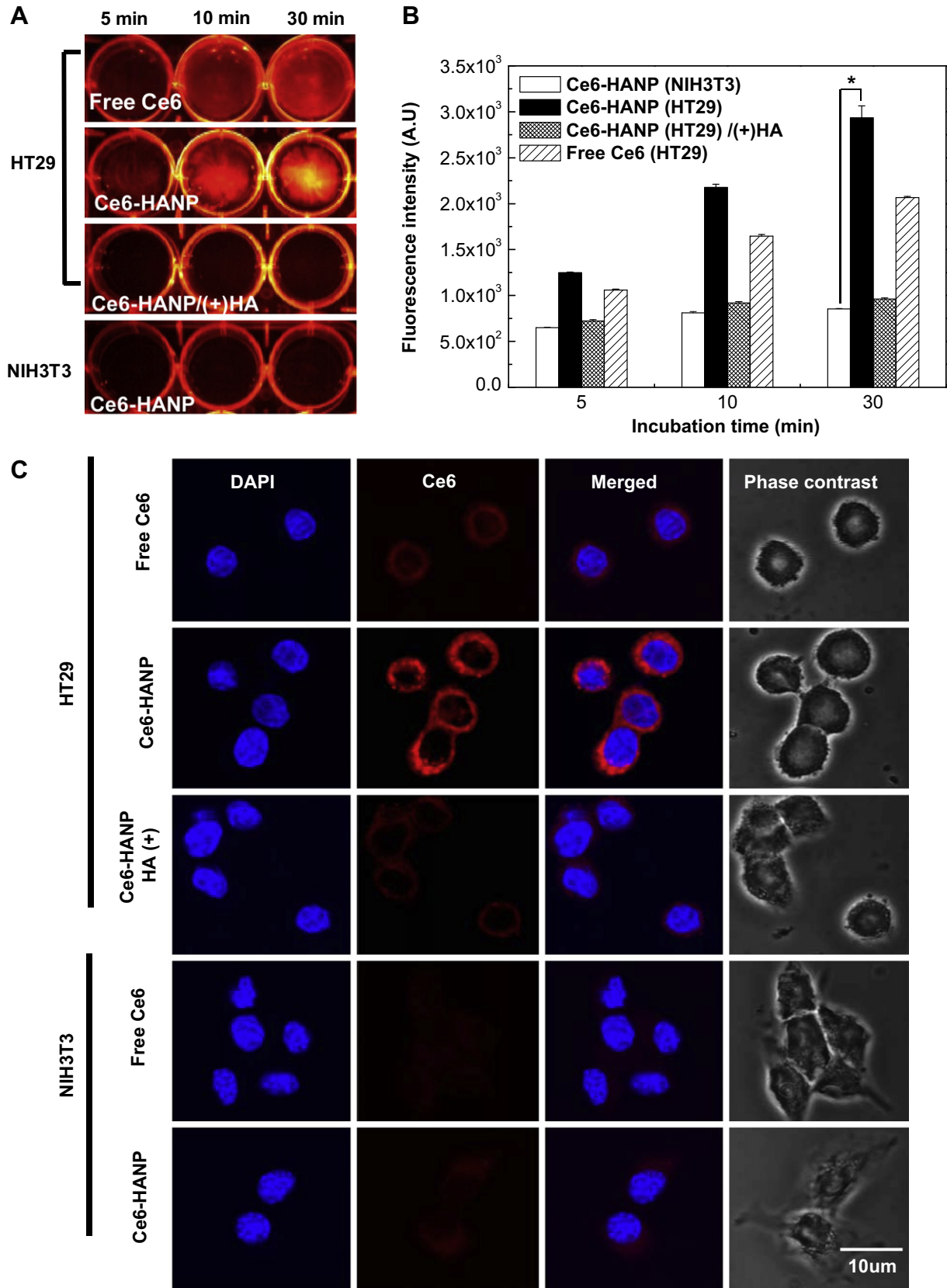


**Fig. 3.** Cellular imaging of Ce6-HANP. (A) Fluorescence images of NIH3T3 and HT29 cells treated with free Ce6 and Ce6-HANP in 6-well plate. (B) Fluorescence intensity of (A). \*indicates difference at the  $p < 0.05$  significance level. (C) Confocal microscopic images of NIH3T3 and HT29 cells treated with free Ce6 and Ce6-HANP.

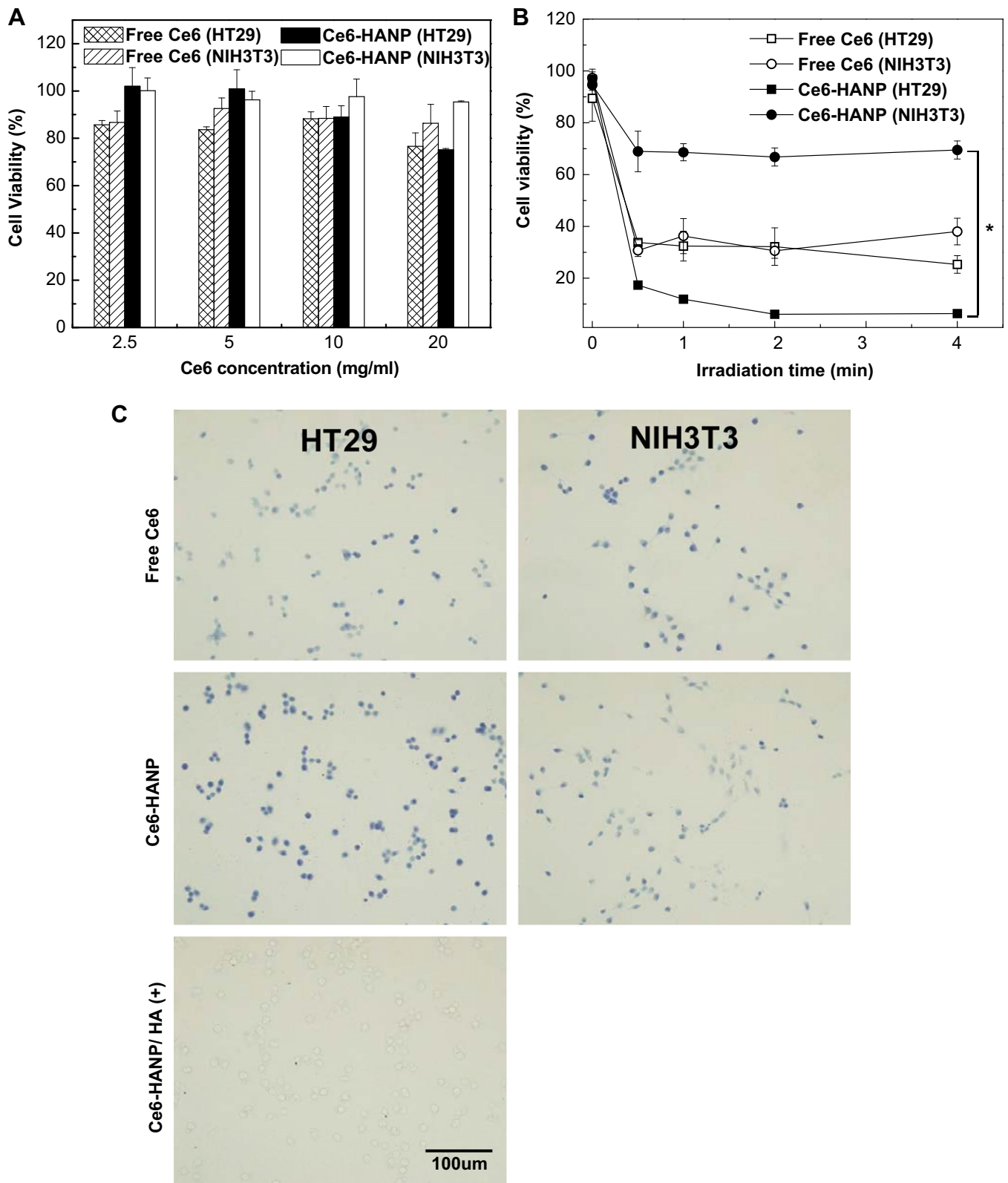


**Fig. 4.** NIR laser-induced phototoxicity of Ce6-HANP. (A) Cell viability of free Ce6 and Ce6-HANP treated cells in dark condition. (B) Cell viability of free Ce6 and Ce6-HANP treated cells after laser irradiation. \*indicates difference at the  $p < 0.05$  significance level. (C) Trypan blue staining images of free Ce6 and Ce6-HANP treated cells after laser irradiation.

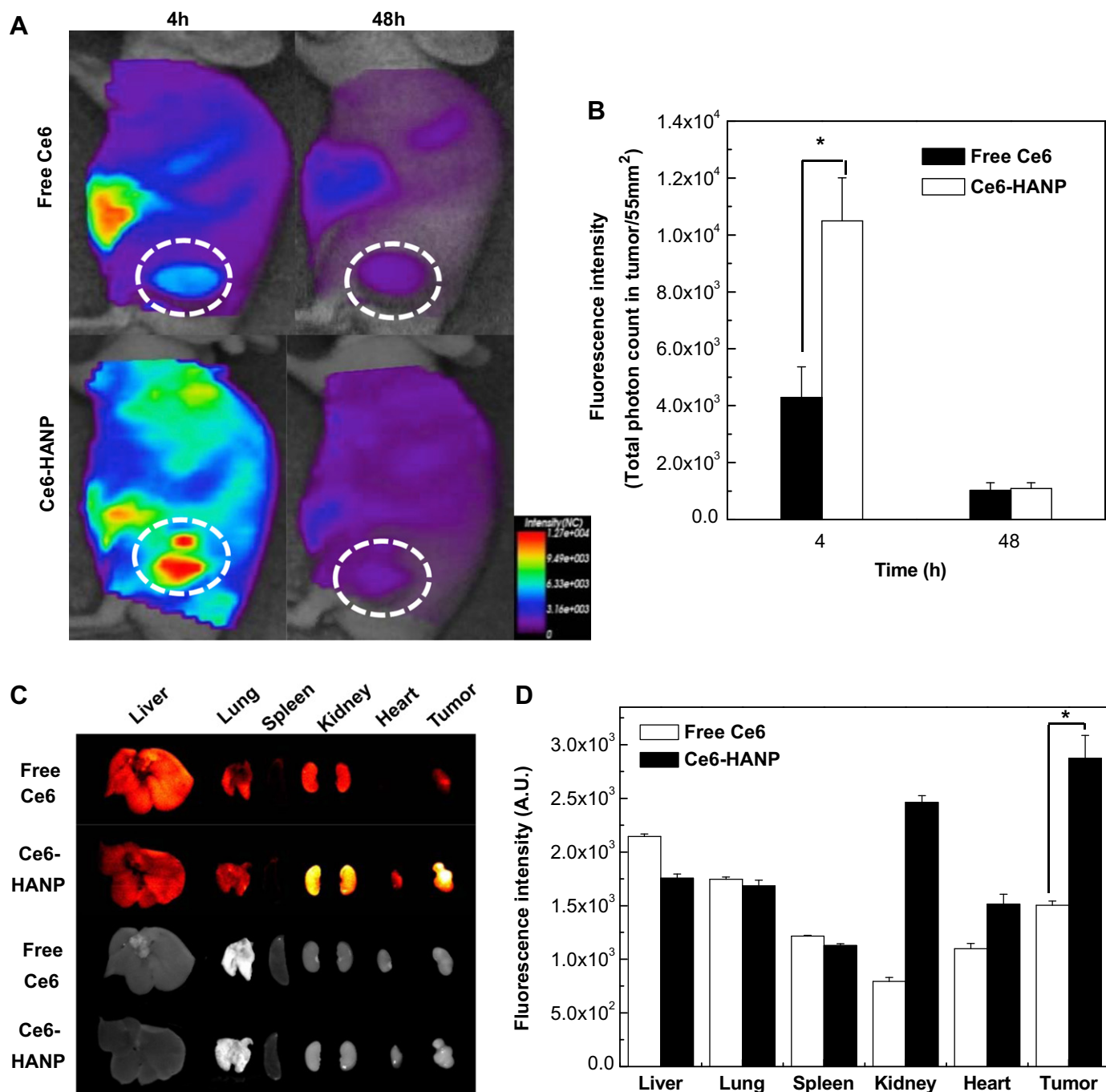


**Fig. 5.** *In vivo* photodynamic imaging with Ce6-HANP. (A) Whole body fluorescence images of HT29 tumor-bearing mice treated with free Ce6 and Ce6-HANP. White circles indicate tumor sites. (B) Total photon counts in tumors of (A). \*indicates difference at the  $p < 0.05$  significance level. (C) *Ex vivo* fluorescence images of organs and tumors in HT29 tumor-bearing mice after 24 h post-injection of free Ce6 and Ce6-HANP. (D) Fluorescence intensities of (C). \*indicates difference at the  $p < 0.05$  significance level.

of Ce6-HANPs to the cancer cell was significantly higher than that of free Ce6, which might be due to the specific cellular uptake and fast release of Ce6 from nanoparticle. This is highly important in clinical point of view, because many nano-carriers showed lower therapeutic efficacy in the cellular condition than free drugs in compensation for the sustained release of drugs [33].

This tumor cell-specific phototoxicity of Ce6-HANPs was also proved in Trypan Blue staining [34]. Trypan Blue is a dye that cannot pass into the cytoplasm of living cells, whereas it is localized inside the damaged or dead cells with membrane permeability. Consequently, its blue colour is an indicator for cellular damage and membrane destruction. In accordance with the results in the MTT

assay, the intense blue spots were shown in Ce6-HANP treated HT29 tumor cells after laser irradiation, compared to NIH3T3 cells and free Ce6-treated HT29 cells. In addition, these spots were not observed after co-treatment of excess HA for competitive cellular uptake proving that the uptake mechanism of Ce6-HANPs was based on receptor (CD44)-mediated endocytosis.

### 3.5. *In vivo* photodynamic imaging

Photosensitizers can generate fluorescence for imaging and cytotoxic singlet oxygen for therapy simultaneously upon irradiation. Therefore, intrinsic fluorescence of photosensitizers allows for

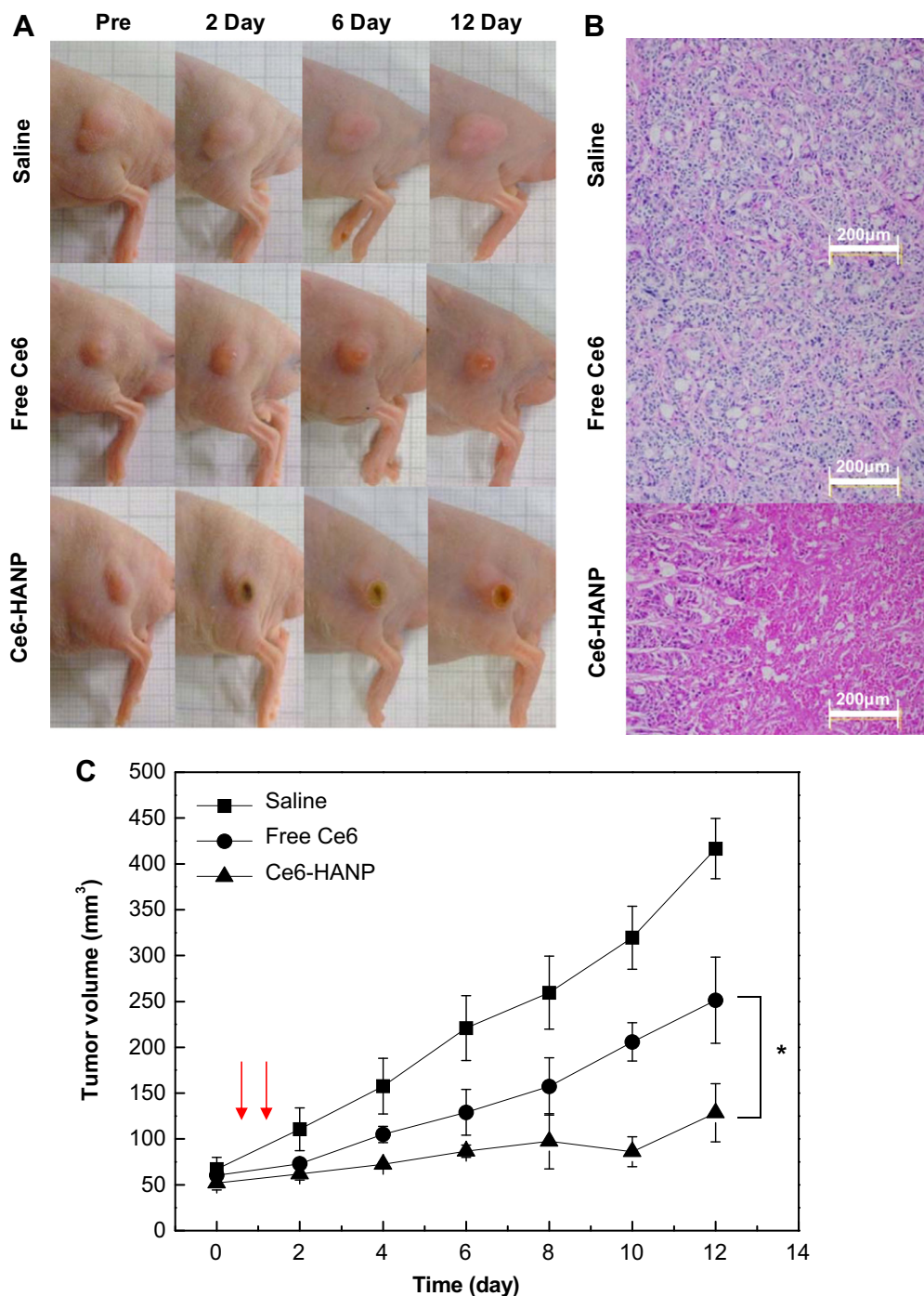


**Fig. 6.** *In vivo* photodynamic therapy with Ce6-HANP. (A) Images of HT29 tumor-bearing mice treated with free Ce6 and Ce6-HANP (5 mg/kg of Ce6) and laser irradiation. (B) Histological tumor tissue images of (A) after H&E staining. (C) Time-dependent tumor growth rate of (A). The arrows indicate the time point for irradiation. \* indicates difference at the  $p < 0.05$  significance level.

evaluating its *in vivo* biodistribution by using the non-invasive optical imaging technique, and tumor-targeted delivery of them can mark the location and area of tumor tissue in whole body [20]. Fig. 5A shows fluorescence images of the tumor-bearing mice after systemic administration of free Ce6 and Ce6-HANPs. The result demonstrated that Ce6-HANPs were effectively accumulated at tumor tissue, compared to free Ce6. Four hours post-injection of Ce6-HANPs, the tumor site emitted intense fluorescence and easily delineated from surrounding tissues proving the possibility for PDT. In addition, most of Ce6 was secreted from the mouse body 48 h post-injection in both free Ce6 and Ce6-HANPs. It meant that Ce6-

HANPs could be almost free from the unintended phototoxicity by remaining photosensitizers after treatment, which is the potential disadvantage of nanoparticulate formulations for PDT. The total photon counts of Ce6 in tumor tissue with Ce6-HANPs was about 2.6 fold higher than that with free Ce6 4 h post-injection (Fig. 5B). The *ex vivo* fluorescence images of excised organs and tumors also confirmed the tumor-targeted delivery of Ce6-HANPs (Fig. 5C). For Ce6-HANPs, the strongest fluorescence signal was found in tumor tissue among organs including liver, spleen, and kidney. However, in mice treated with free Ce6, the strongest signal was found in liver. The fluorescence intensity of excised tumor with Ce6-HANPs

was 1.8 fold higher than that of free Ce6 after 24 h (Fig. 5D). The high intensity in kidney was also observed in Ce6-HANPs treated mouse. We thought that it was not a serious problem because kidney is a major excretory organ and filtered molecules are rapidly removed from the body by urine [35].

### 3.6. *In vivo* photodynamic therapy

In an attempt to evaluate the therapeutic potential, we injected saline, free Ce6, and Ce6-HANPs (5 mg/kg of Ce6) into HT29 tumor-bearing mice via the tail vein. Thereafter, tumor sites of all mice were irradiated using the NIR laser for 30 min. After irradiation, there was a clear hemorrhagic injury in the tumor sites of mice treated with Ce6-HANPs, implying effective tumor therapy (Fig. 6A). From the free Ce6-treated mice, it was found that the tumor was partially damaged after irradiation and was regrown after 12 days. The histological tissue images, obtained by H&E staining, also demonstrated the high therapeutic efficacy of Ce6-HANPs (Fig. 6B). A large amount of cell death in tumor tissue was observed in the mice treated with Ce6-HANPs. However, cell death was relatively rare in the mice treated with saline or free Ce6. The therapeutic efficacy was also evaluated by comparing the tumor growth rate of three groups including the mice treated with saline, free Ce6, and Ce6-HANPs (Fig. 6C). The size of tumors in free Ce6-treated mice was 250 mm<sup>3</sup> after 12 days, and this value is 59% of the saline-treated mice. On the other hand, the growth of tumor tissue was successfully suppressed by Ce6-HANPs. The final mean size of tumors in Ce6-HANPs treated mice was 120 mm<sup>3</sup>, which is only 27% of the saline-treated control group. This enhanced therapeutic efficacy originates from the high accumulation and dequenching of Ce6-HANPs in tumor tissue, followed by vigorous production of singlet oxygen upon irradiation. Overall, these results demonstrated that Ce6-HANPs are highly useful for PDT of tumors.

## 4. Conclusion

Tumor-targeting hyaluronic acid nanoparticles containing Ce6 (Ce6-HANPs) were prepared in this study, and they were explored for simultaneous photodynamic imaging and therapy. It was found that Ce6 could be rapidly released from Ce6-HANPs through degradation of the HA backbone in the presence of hyaluronidase abundant in cytosol of tumor cells. The released Ce6 was quenched and generated fluorescence and singlet oxygen upon NIR laser irradiation. The tumor-targeted delivery of Ce6-HANPs based on both passive and active targeting was proved by non-invasive *in vivo* imaging. In tumor-bearing mice models, Ce6-HANPs could effectively suppress the tumor growth compared to free Ce6. In conclusion, Ce6-HANPs can be successfully applied to *in vivo* photodynamic imaging and therapy in cancer treatment, simultaneously.

## Acknowledgements

This work was financially supported by the Global Research Laboratory (GRL) Project, the Fusion Technology Project (2009-0081876), and the Basic Science Research Programs (20100027955 and 20100015804) of MEST, and the Intramural Research Program (Theragnosis) of KIST.

## References

- Jain RK, Stylianopoulos T. Delivering nanomedicine to solid tumors. *Nat Rev Clin Oncol* 2010;7:653–64.
- Koo H, Huh MS, Ryu JH, Lee D-E, Sun I-C, Choi K, et al. Nanoprobes for biomedical imaging in living systems. *Nano Today* 2011;6:204–20.
- Kobayashi H, Choyke PL. Target-cancer-cell-specific activatable fluorescence imaging probes: rational design and *in vivo* applications. *Acc Chem Res* 2010;44:83–90.
- Lee S, Park K, Kim K, Choi K, Kwon IC. Activatable imaging probes with amplified fluorescent signals. *Chem Commun (Camb)*; 2008:4250–60.
- Delcea M, Möhwald H, Skirtach AG. Stimuli-responsive LbL capsules and nanoshells for drug delivery. *Adv Drug Del Rev* 2011;63:730–47.
- Petros RA, DeSimone JM. Strategies in the design of nanoparticles for therapeutic applications. *Nat Rev Drug Discov* 2010;9:615–27.
- Park K, Lee S, Kang E, Kim K, Choi K, Kwon IC. New generation of multifunctional nanoparticles for cancer imaging and therapy. *Adv Funct Mater* 2009;19:1553–66.
- Koo H, Huh MS, Sun I-C, Yuk SH, Choi K, Kim K, et al. *In vivo* targeted delivery of nanoparticles for theranosis. *Acc Chem Res* 2011;44:1018–28.
- Choi KY, Min KH, Na JH, Choi K, Kim K, Park JH, et al. Self-assembled hyaluronic acid nanoparticles as a potential drug carrier for cancer therapy: synthesis, characterization, and *in vivo* biodistribution. *J Mater Chem* 2009;19:4102–7.
- Choi KY, Chung H, Min KH, Yoon HY, Kim K, Park JH, et al. Self-assembled hyaluronic acid nanoparticles for active tumor targeting. *Biomaterials* 2010;31:106–14.
- Maeda H, Wu J, Sawa T, Matsumura Y, Hori K. Tumor vascular permeability and the EPR effect in macromolecular therapeutics: a review. *J Control Release* 2000;65:271–84.
- Lapčič L, De Smedt S, Demeester J, Chabreček P. Hyaluronan: Preparation, properties, and applications. *Chem Rev* 1998;98:2663–84.
- Clevers H. The cancer stem cell: premises, promises and challenges. *Nat Med*; 2011:313–9.
- Ishimoto T, Nagano O, Yae T, Tamada M, Motohara T, Oshima H, et al. CD44 variant regulates redox status in cancer cells by stabilizing the xCT subunit of system xc- and thereby promotes tumor growth. *Cancer Cell* 2011;19:387–400.
- Stern R, Jedrzejewski MJ. Hyaluronidases: their genomics, structures, and mechanisms of action. *Chem Rev* 2006;106:818–39.
- Szarpak A, Cui D, Fdr Dubreuil, De Geest BG, De Cock LJ, Picart C, et al. Designing hyaluronic acid-based layer-by-layer capsules as a carrier for intracellular drug delivery. *Biomacromolecules* 2010;11:713–20.
- Choi KY, Min KH, Yoon HY, Kim K, Park JH, Kwon IC, et al. PEGylation of hyaluronic acid nanoparticles improves tumor targetability *in vivo*. *Biomaterials* 2011;32:1880–9.
- Celli JP, Spring BQ, Rizvi I, Evans CL, Samkoe KS, Verma S, et al. Imaging and photodynamic therapy: mechanisms, monitoring, and optimization. *Chem Rev* 2010;110:2795–838.
- Thakare VS, Das M, Jain AK, Patil S, Jain S. Carbon nanotubes in cancer theragnosis. *Nanomedicine* 2010;5:1277–301.
- Koo H, Lee H, Lee S, Min KH, Kim MS, Lee DS, et al. *In vivo* tumor diagnosis and photodynamic therapy via tumoral pH-responsive polymeric micelles. *Chem Commun* 2010;46:5668–70.
- Na JH, Koo H, Lee S, Min KH, Park K, Yoo H, et al. Real-time and non-invasive optical imaging of tumor-targeting glycol chitosan nanoparticles in various tumor models. *Biomaterials* 2011;32:5252–61.
- Lee SJ, Park K, Oh Y-K, Kwon S-H, Her S, Kim I-S, et al. Tumor specificity and therapeutic efficacy of photosensitizer-encapsulated glycol chitosan-based nanoparticles in tumor-bearing mice. *Biomaterials* 2009;30:2929–39.
- Choi KY, Yoon HY, Kim J-H, Bae SM, Park R-W, Kang YM, et al. Smart nano-carrier based on PEGylated hyaluronic acid for cancer therapy. *ACS Nano* 2011;5:8591–9.
- Park W, Park S-J, Na K. The controlled photoactivity of nanoparticles derived from ionic interactions between a water soluble polymeric photosensitizer and polysaccharide quencher. *Biomaterials* 2011;32:8261–70.
- Lovell JF, Liu TWB, Chen J, Zheng G. Activatable photosensitizers for imaging and therapy. *Chem Rev* 2010;110:2839–57.
- Gurinovitch GP, Zorina TE, Melnov SB, Melnova NI, Gurinovitch IF, Grubina LA, et al. Photodynamic activity of chlorin e6 and chlorin e6 ethylenediamide *in vitro* and *in vivo*. *J Photochem Photobiol B Biol* 1992;13:51–7.
- Weissleder R. A clearer vision for *in vivo* imaging. *Nat Biotechnol* 2001;19:316–7.
- Torchilin V. Tumor delivery of macromolecular drugs based on the EPR effect. *Adv Drug Deliv Rev* 2011;63:131–5.
- Itano N. Simple primary structure, complex turnover regulation and multiple roles of hyaluronan. *J Biochem* 2008;144:131–7.
- Kramer MW, Escudero DO, Lokeshwar SD, Golshani R, Ekwenna OO, Acosta K, et al. Association of hyaluronic acid family members (HAS1, HAS2, and HYAL-1) with bladder cancer diagnosis and prognosis. *Cancer* 2011;117:1197–209.
- Ekici S, Cerwinka WH, Duncan R, Gomez P, Civantos F, Soloway MS, et al. Comparison of the prognostic potential of hyaluronic acid, hyaluronidase (HYAL-1), CD44v6 and microvessel density for prostate cancer. *Int J Cancer* 2004;112:121–9.
- Morgan J, Oseroff AR. Mitochondria-based photodynamic anti-cancer therapy. *Adv Drug Deliv Rev* 2001;49:71–86.
- Duncan R. Polymer conjugates as anticancer nanomedicines. *Nat Rev Cancer* 2006;6:688–701.
- Yi DK, Sun I-C, Ryu JH, Koo H, Park CW, Yoon I-C, et al. Matrix metalloproteinase sensitive gold nanorod for simultaneous bioimaging and photothermal therapy of cancer. *Bioconj Chem* 2010;21:2173–7.
- Masereeuw R, Russel FGM. Mechanisms and clinical implications of renal drug excretion. *Drug Metab Rev* 2001;33:299–351.